Materials & Design 236 (2023) 112453

Contents lists available at ScienceDirect

Materials & Design

journal homepage: www.elsevier.com/locate/matdes

Near-surface defect detection in additively manufactured components using laser induced phased arrays with surface acoustic wave crosstalk suppression

Geo Davis [a,*], Theodosia Stratoudaki [a,*], Peter Lukacs [a], Matthew W. Riding [a], Ahmed Al Fuwaires [a], Panagiotis Kamintzis [a], Don Pieris [a], Alan Keenan [a], Paul Wilcox [b], Gareth Pierce [a], Charles MacLeod [a], Stewart Williams [c]

[a] Department of Electronic and Electrical Engineering, University of Strathclyde, Glasgow, G1 1XQ, United Kingdom
[b] Department of Mechanical Engineering, University of Bristol, Bristol, BS8 1Q, United Kingdom
[c] Welding and Additive Manufacturing Centre, Cranfield University, Cranfield, MK43 0AL, United Kingdom

ARTICLE INFO

Dataset link: https://doi.org/10.15129/0cfd48c9-733d-4636-8f0a-b28bf48a34bd

Keywords:
Additive manufacturing
Laser induced phased arrays
Wave suppression
Total focusing method
Ultrasonic near-surface defect imaging

ABSTRACT

In-process inspection of the additive manufacturing process requires a technique that can provide reliable measurements given the extreme operating environments, the small size of the defects and the cyclic melting and heating of the material, caused by subsequently deposited layers. A remote and couplant-free ultrasonic inspection technique using bulk waves that can image near-surface defects could address these in-process inspection requirements. Laser induced phased arrays (LIPA) generate and detect ultrasound based on laser ultrasonics principles, while the array is synthesised in post-processing. However, when using LIPAs for inspection, the surface acoustic waves (SAWs) interfere with the bulk wave modes giving rise to crosstalk and artefacts, which makes near-surface defect imaging difficult. This work experimentally validates and compares five techniques for SAW suppression: amplitude thresholding, mean waveform subtraction, principal component subtraction, frequency-wavenumber filtering, and phase coherence imaging. SAW suppression is demonstrated in ultrasonic images of transverse waves based on 71-element LIPA data synthesised on a Ti-6Al-4V directed energy deposition-arc (DED-Arc/Ti6Al4V) sample with a ~1 mm diameter side drilled hole, located at ~4 mm below the inspected surface. The reported results show that the principal component subtraction approach achieved the highest 'signal-to-crosstalk ratio' improvement of 16 dB, while successfully suppressing the SAW.

1. Introduction

In-process non-destructive evaluation (NDE) is particularly important for AM components addressing the needs of high-value manufacturing, such as aerospace or power generation applications. Robustness of manufacturing and reliability of the end product are paramount in such applications, which have to adhere to strict quality standards [1–5]. At the moment, NDE of such components takes place at the end of manufacturing, mainly using X-ray and ultrasound inspection. The latter is delivered either through contact or immersion based ultrasonic systems, using ultrasonic transducers or transducer arrays. Both X-rays and transducer-based ultrasonics are not suitable for in-process inspection. However, an in-process inspection system would result in significant cost and material reductions if a defect in the structure was able to be detected as soon as it occurred. This in-process NDE approach would also give a chance for remedial action to take place, from the point of manufacturing, if this were possible [6–9].

Optical based techniques are best suited for in-process NDE: light can sense remotely, addressing the hot temperatures associated with AM, and its small footprint suits well for complex geometries. However, optical based techniques are usually limited to examining the near surface. Ultrasound on the other hand can probe the inner structure of materials, but conventional ultrasonic transducers require contact, an ultrasound coupling medium, are relatively bulky and cannot withstand high temperature environments. Laser ultrasound (LU) circumvents these issues: pulsed lasers are used remotely and without ultrasonic coupling medium for ultrasonic excitation of all wave modes (bulk and surface waves). This is done through optical absorption of ir-

* Corresponding author.
E-mail addresses: geo.davis@strath.ac.uk (G. Davis), t.stratoudaki@strath.ac.uk (T. Stratoudaki).

https://doi.org/10.1016/j.matdes.2023.112453
Received 20 July 2023; Received in revised form 13 October 2023; Accepted 5 November 2023
Available online 20 November 2023

radiation and thermal expansion or ablation of the material, creating elastic waves [10]. These waves travel through the bulk or the surface and are detected remotely by lasers (usually by means of optical interferometry [11]) after their interaction with the propagating medium. The remote delivery of the technique gives laser ultrasound the potential for in-process, remote sensing of AM, allowing layer-by-layer ultrasound inspection of the AM built structure.

Examples of the potential of laser based ultrasound for in-process inspection of AM can be found here [12–15]. Cerniglia et al., [12] demonstrated a proof-of-concept prototype of laser ultrasonic technique for in-process inspection of directed energy deposition-laser beam (DED-LB) components. The laser system was mounted on the DED-LB robot and scanned to acquire ultrasonic data. Side drilled holes (SDH) representing defects with diameters in the range 154 μm - 500 μm and at depths ranging from 13 μm - 800 μm were inspected using the system. The disruption of the surface acoustic wave (SAW) was the main mechanism by which the flaws were detected. However, the authors report that the sensitivity of the technique decreased significantly for flaws 100 μm below the surface. Another state-of-the-art laser based technique that can be used for in-process inspection of AM components is the spatially resolved acoustic spectroscopy (SRAS). SRAS uses wavelength-constrained comb excitation of surface acoustic waves to obtain velocity map of the scanned surface [14]. SRAS enables rapid imaging of material microstructure and grain orientation. Smith et al., [15] also reports on using SRAS for defect detection. Micro pores in the size range 115 μm - 119 μm up to a maximum depth of 24 μm were imaged on a powder bed fusion-laser beam (PBF-LB) component. Dryburgh et al., [13] reported on utilising SRAS to image undeformed and rolled directed energy deposition-arc (DED-Arc) specimens, in both polished and as-deposited states. Their work proposes a basic algorithm for automated measurement, which could be used for in-process closed-loop control of the DED-Arc process. However, the techniques discussed above [12–15] are limited to surface and near-surface imaging where the imaging depths are within the re-melting and re-heating zone of the AM processes and hence the microstructure and defects imaged are likely to change due to re-melting and re-heating when the next layer is deposited.

LU-based defect imaging in AM components, using bulk waves, has also been performed. For example, Lévesque et al., [16,17] combined LU and synthetic aperture focusing technique (SAFT) to image porosities in AM components using the longitudinal wave arrival. Zeng et al., [18] used LU generated and detected SAW and transverse waves, in a pitch-catch configuration, to image a 2 mm diameter SDH in a DED-Arc sample, using B-scan. Davis et al., [19] performed laser ultrasonic testing in a through-transmission setting using longitudinal waves on an AM component to image SDHs using B-scans and C-scans. The above imaging approaches were limited to B-scans, C-scans and SAFT. Laser induced phased arrays (LIPAs), have been developed for remote, couplant-free NDE [20–22] and we have shown that using imaging algorithms such as the total focusing method (TFM), higher quality imaging can be achieved compared to B-scan or SAFT [20,23,24].

LIPAs are based on the principles of laser ultrasonics where pulsed lasers are used for remote, couplant-free ultrasonic excitation and detection of all wave modes (bulk and surface waves) [10]. In a LIPA, the array is synthesised and the beamforming is done in post-processing. LIPAs have superior ultrasonic imaging performance over conventional LU techniques because they can mitigate the low signal-to-noise ratio (SNR) associated with LU when working in the non-ablative regime by synthetic focusing and steering of the ultrasonic beam. This is done through capturing the full matrix [25] which allows the use of a range of ultrasonic imaging algorithms, such as the TFM, which is currently considered the golden standard in ultrasonic imaging [25]. Using these modern paradigms of ultrasonics, we have demonstrated the capabilities of LIPAs by ultrasonically imaging nested features within AM components, paving the way for in-process inspection [22]. As part of this study, LIPAs were shown to be able to image cylindrical features, as small as 0.2 mm, printed using PBF-LB of aluminium, located 26 mm below the scanned surface [22]. We have also presented ultrasonic imaging of a Ti-6Al-4V DED-Arc-built component with 1 mm SDHs located 10 mm below the scanned surface [26].

Table 1
Table showing typical dimensions of common defects that occur during the PBF-LB and DED-Arc process.

Defects	Typical sizes PBF-LB (μm)	Typical sizes DED-Arc (μm)
Porosity	5 - 20 [6]	126 - 286 (Ti-6Al-4V) [27] 5 - 75 (Al alloy) [28]
Lack of fusion	50 - 500 [6]	20 - 30 (Between layers) [9]
Unfused powder	100 - 150 [6]	Not applicable

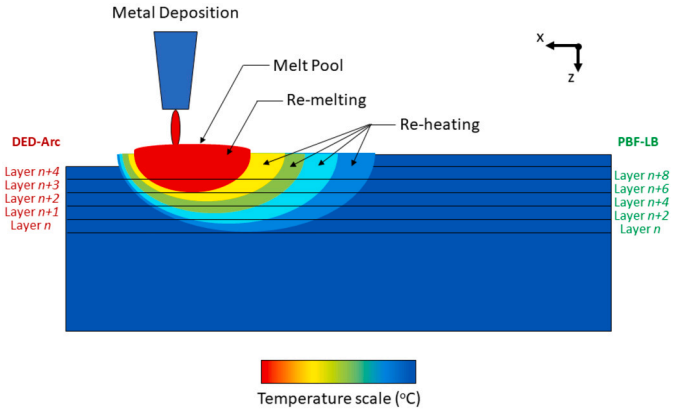

Fig. 1. Schematic cross-sectional representation of a typical AM build as a snapshot in time, showing the temperature gradients within the build for both the DED-Arc and PBF-LB processes in terms of deposited layers.

The requirements for in-process inspection of AM components, with respect to the size of defects encountered, are shown in Table 1 for PBF-LB and DED-Arc AM processes. Linking the information in this table to the current capabilities of LIPAs for defect detection, it can be seen that the technique would be able to detect some porosity (DED-Arc) and lack of fusion (PBF-LB) defects. In general, a suitable ultrasonic technique should be able to successfully detect defects of this size and this ability is related to the ultrasonic frequency excited. In LU, this is related to the laser pulse width, which typically is 5-20 ns, corresponding to a broadband ultrasonic excitation of 0-200 MHz and would be sufficient to detect sub-millimetre size defects. Another set of NDE requirements is set by the nature of the AM process during metal deposition. Fig. 1 shows a cross-sectional, general representation of the temperature gradients present during the AM process, where depth is shown as a function of deposition layers for DED-Arc [29] and PBF-LB [30], based on published data.

The representation in Fig. 1 is a snapshot of a dynamic process and as the metal deposition source is moving, the location of the thermal gradient will be moving along. The representation shows that several deposited layers (not just the top one) are undergoing cyclic heating and cooling and the material is subject to cyclic change [29,30]. In practice, this means that any defects formed at the last deposited layer, may or may not be present when this cyclic heat treatment has subsided. The deposited layers affected are around five for DED-Arc and ten for PBF-LB and depend on the type of AM process and the specific conditions of metal deposition (see references included in Table 2). Some typical numbers of the deposited layer thickness are shown in Table 2. Ideally, the NDE system should be able to detect defects at depths greater than 0.2 mm for PBF-LB or 5 mm for DED-Arc, below the last deposited surface. These requirements regarding the defect size and location dictate the need for bulk wave inspection of AM relevant defects. As an example, taking into account the ultrasonic resolution required by the

Table 2
PBF-LB and DED-Arc layer characteristics.

	PBF-LB [30]	DED-Arc [29]
Typical deposited layer thickness (μm)	20 - 60	1000 - 2000
Re-melting zone (number of layers)	4	2
Re-heating zone (number of layers)	10	5

typical defect sizes, these dictate that we should be working roughly with ultrasonic waves > 12 MHz for transverse waves.

In-process ultrasonic inspection should be able to detect defects below the last deposited 10 layers for PBF-LB and 5 layers for DED-Arc. This requirement calls for ultrasonic inspection using bulk waves because surface acoustic waves (SAWs) with penetration depth at these values (i.e. >0.2 mm for PBF-LB and >5 mm for DED-Arc) would need to be of too low ultrasonic frequency and unable to address the sizing requirements of the inspection, as shown in Table 1 (i.e. >12 MHz and >20 MHz for PBF-LB and DED-Arc respectively). This is because the penetration depth of the SAW is limited to around one ultrasonic wavelength [31].

The laser ultrasonic generation mechanism excites simultaneously SAW and bulk waves [10]. As a result, there is a crosstalk region where SAWs will arrive at the detection point at the same expected time of arrival as waves travelling in the bulk. This crosstalk region is confined to the area close to the surface and extending to a certain depth, which depends on the aperture size (A) of the LIPA, the ultrasonic velocity of the SAW (c_R) and the ultrasonic velocity of the bulk wave (c_B) in the material, as will be explained in section 2.2.

If we are using LIPAs for in-process inspection during AM deposition, then typical values for A, c_R, and c_B mean that ultrasonic imaging for possible defects is required at near-surface depths, where SAW crosstalk is more likely to be present. Therefore, the objective of this paper is to present and experimentally validate possible methods for: a) suppressing the SAW crosstalk and b) compare the effectiveness of these methods for successful ultrasonic imaging of near-surface defects in AM related material.

This paper presents and compares five techniques for SAW crosstalk suppression. These techniques target the unique characteristics of the SAW, such as its ultrasonic amplitude (amplitude thresholding), waveform shape (mean waveform and principal component subtraction), ultrasonic velocity (frequency - wavenumber filtering) and phase (phase coherence imaging).

The paper has the following structure: section 2 gives a brief background on how LIPAs are synthesised based on the full matrix capture (FMC) data acquisition method and the TFM imaging algorithm; the section also describes the phenomenon of SAW crosstalk in detail; section 3 presents the experimental setup, data acquisition conditions and DED-Arc component used in this study; section 4 presents the theory of each SAW crosstalk suppression method; section 5 presents experimental results and comparison of each method; section 6 presents the conclusions and future potential arising from this work.

2. Background

This section details the necessary background information required to understand the techniques and approaches considered in this paper. This section first introduces the concept of LIPAs followed by the FMC data acquisition strategy and the TFM imaging algorithm. This section concludes by describing the surface acoustic wave crosstalk.

2.1. Laser induced phased arrays, full matrix capture and total focusing method

LIPAs are ultrasonic arrays synthesised in post-processing where the ultrasound is generated and detected by lasers [20,32].

In the results presented in this paper, the FMC data acquisition method is used, which means that ultrasonic signals from all possible combinations of ultrasonic generation and detection positions of array elements, are acquired [25]. Following the FMC data acquisition, the envelope (Hilbert transform) of the ultrasonic signal is extracted and then a frequency-domain, Gaussian digital filter is applied, followed by inverse transformation of the positive half of the filtered signals [20]. Digital filtering is applied to the data in order to remove the low-frequency ambient noise components, and also the high-frequency electronic noise and the material microstructure-induced scattering noise from the ultrasonic signal [33].

The FMC dataset allows for a variety of imaging algorithms to be applied during post-processing including the TFM. The TFM algorithm used in this paper is the same applied for transducer phased arrays [20,25]. In TFM, the acquired signals are focused at every point in the image, in post-processing, by applying a delay-and-sum algorithm [34]. The TFM algorithm is implemented as follows. First, an image frame is considered that represents the cross-section of the sample to be imaged. The image frame is then discretised into a grid consisting of pixels. For each pixel, the ultrasonic signals from every generation-detection pair combination are summed using the appropriate time delay. The intensity of the TFM image, $I(\mathbf{r})$, at any position $\mathbf{r}=[x,z]$ is given by [25]:

$$I(\mathbf{r}) = \left| \sum_{T=1}^{N} \sum_{R=1}^{N} S_{TR}(t_{TR}(\mathbf{r})) \right| \tag{1}$$

where 'T' represents the generation elements and 'R' represents the detection elements. 'N' is the total number of array elements. The variable $S_{TR}(t)$ is the ultrasonic signal for the corresponding 'T' and 'R' combination and t_{TR} is the time delay, which is given by:

$$t_{TR} = \frac{d_T(\mathbf{r}) + d_R(\mathbf{r})}{c_B} \tag{2}$$

where $d_T(\mathbf{r})$ and $d_R(\mathbf{r})$ are the ray-path distances associated with the generation and detection elements to a point $\mathbf{r}$ in the image frame. c_B is the bulk wave velocity.

Due to its ability to use every possible ultrasonic signal from an array and achieve focusing on every pixel in the image, TFM achieves significantly higher SNR than other conventional imaging methods such as the plane B-scan and the focused B-scan [25,20]. The TFM images are normalised to the defect intensities, and the intensities are converted to decibels according to the following equation:

$$I_{dB} = 20 \log_{10} \frac{I(\mathbf{r})}{I_{max}} \tag{3}$$

where $I(\mathbf{r})$ is given by equation (1) and I_{max} has the value corresponding to the maximum intensity at the location of the defect.

2.2. Surface acoustic wave crosstalk

In laser ultrasonics, SAWs, bulk longitudinal waves and bulk transverse waves are generated at the same instant in a material [10]. However, SAWs are generated with the highest amplitude among the wave modes (see Fig. 2(a)) [35].

SAWs propagate slower compared to the bulk longitudinal and transverse waves, while they travel a shorter path between the transmitter and the receiver, in most metals. Hence, in LIPA, for a few generation-detection element combinations, the bulk wave reflected from an internal feature and the SAW arrive at the detection point at the same expected time (see Fig. 2). This happens when the internal feature is sufficiently close to the surface. In this case, the SAW wave mode, with its high amplitude, overwhelms the bulk wave modes that may arrive at the same instant; hence this is termed as SAW crosstalk. When imaging using bulk waves, the SAW crosstalk over-saturates a region near the surface and beneath the array location, making it difficult to detect near-surface defects using LIPAs.

The SAW crosstalk phenomenon is explained in Fig. 2(b). T_n and R_m are the transmit and receive elements respectively. The 'green' and 'red'

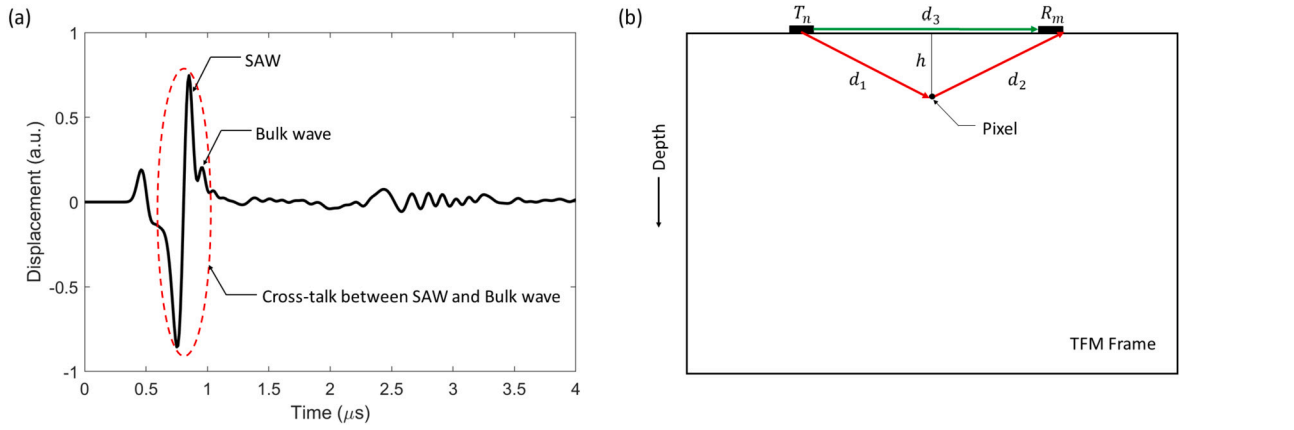

Fig. 2. (a) Finite element simulation generated ultrasonic signal showing the temporal SAW crosstalk phenomenon, (b) schematic demonstrating the principle of temporal SAW crosstalk.

arrows represent the path taken by the SAW and bulk wave mode respectively. d_1 is the distance travelled by the bulk wave mode from T_n to the pixel, and d_2 is the distance travelled by the bulk wave mode from the pixel to R_m. d_3 is the distance travelled by the SAW mode on the surface from the T_n to the R_m. SAW crosstalk occurs for the T_n-pixel-R_m combination shown, when the time taken by the SAW to travel the distance d_3 is equal to the time taken by the bulk wave mode to travel the distance $d_1 + d_2$. This is represented by the following equation:

$$\frac{d_1 + d_2}{c_B} = \frac{d_3}{c_R} \tag{4}$$

The limiting value of d_3 is the full aperture (A) of the array and hence the time for the SAW to travel the full aperture is:

$$t_c = \frac{A}{c_R} \tag{5}$$

which also provides the maximum depth in an image at which the crosstalk will occur:

$$h = \frac{1}{2}\sqrt{(t_c \cdot c_B)^2 - A^2} \tag{6}$$

For a simplified example, in the experiments considered in this study, a LIPA aperture of 14 mm was synthesised and the acoustic velocities for Ti-6Al-4V (as measured from the experimental data presented in this paper) were 5866 m/s, 3233 m/s, and 3015 m/s for the longitudinal, transverse, and the SAW respectively. Substituting these values in equation (6) gives the maximum depth of SAW crosstalk as 2.7 mm and 11.7 mm for transverse wave mode based imaging and longitudinal wave mode based imaging respectively. However, the SAW crosstalk is more pronounced in transverse wave mode based TFM imaging since the transverse wave and SAW velocities are more similar (3233 m/s and 3015 m/s respectively, for Ti-6Al-4V) compared to the longitudinal mode velocity, and the maximum crosstalk depth (h) is shallower. Consequently, the SAW crosstalk affected area is smaller and the SAW energy is more dense. This is the reason why we present the SAW suppression analysis for the case of TFM imaging using transverse waves.

Artefacts due to SAW signals will also appear in the TFM images when performing ultrasonic imaging using LU data. For example, consider the case where a TFM image is generated using the transverse wave mode. While the TFM algorithm is applied using transverse velocity, other wave modes, such as the SAW and the longitudinal wave, are generated and are present in the ultrasonic signals. Thus, out-of-focus, multi-modal artefacts will occur at incorrect positions on the TFM images, similar to artefacts induced by mode-converted waves appearing in TFM using data from transducer based phased arrays [36]. This is the case with the TFM pixels close to the surface. The SAW will be summed

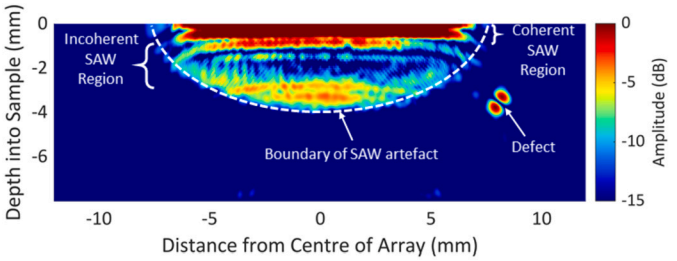

Fig. 3. TFM image using transverse wave velocity showing the various regions of SAW artefact from a Ti-6Al-4V sample. The image was acquired using a 71 element LIPA of 14 mm aperture.

coherently for these pixels albeit out of focus (due to the difference in velocity), as the surface is the place of origin of the SAWs. The SAWs are incoherent for pixels within the bulk of the sample because they originate at the surface. This incoherence means that the SAW signals are out of phase with each other at pixels that are not on the surface, thus they destructively interfere with each other in the TFM algorithm. At the boundary of the crosstalk region, there will be a residual SAW signal in the TFM images. This is due to the SAW signals from the array elements located at the edges of the array aperture, as there are no more SAW to be summed beyond this point. Fig. 3 shows the presence of the artefact regions induced by the SAW in a TFM image using LIPA data and the transverse wave velocity. As shown in the figure, the artefact due to SAW is observed up to a depth of 4 mm. If defects are present at a depth shallower than that defined by equation (6), they will appear within this SAW artefact region, rendering defect detection challenging. In fact, the worst-case scenario for defect detection within the crosstalk region, is when the defect is at the boundary, and this is the case examined in this study. When using LIPAs during AM deposition, such near-surface depths are of great interest for imaging possible defects since these depths fall just outside the re-melting and re-heating zones, as discussed in section 1.

3. Materials and methods

This section describes the experimental setup used for the laser induced phased array experiments, the AM sample used and its fabrication method, and the approaches considered for SAW suppression.

3.1. Experimental setup

The experimental setup is shown in Fig. 4 and consists of one laser for ultrasound generation (shown as red beam in Fig. 4) and another

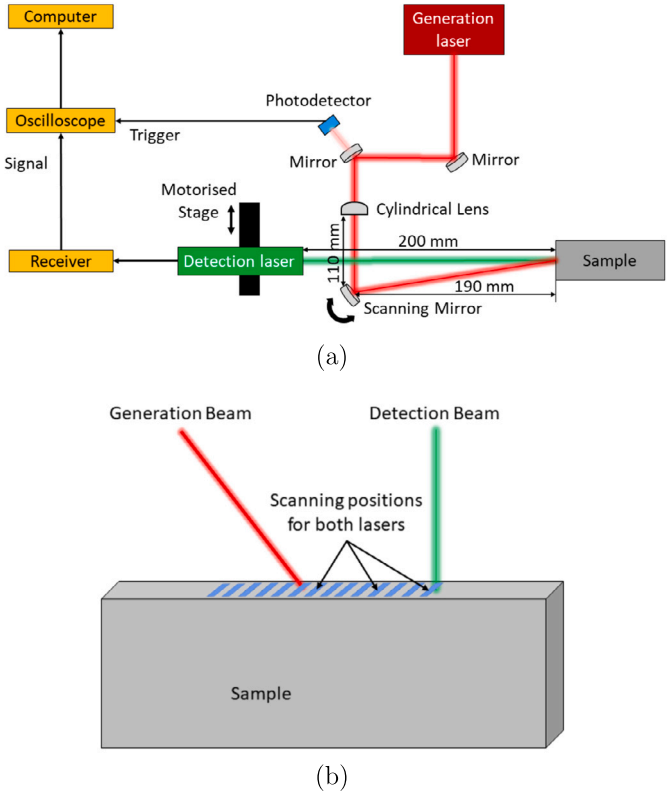

Fig. 4. (a) Schematic of the experimental setup used in this study. (b) Schematic of the sample illustrating the scanning positions of the generation laser beam and detection laser beam.

laser for ultrasound detection (shown as green beam in Fig. 4). The generation laser is a pulsed, Ytterbium-doped fiber laser, emitting at 1064 nm wavelength (TruPulse 2005 nano, FK10-EP, UK).

The laser ultrasonic detection system is a rough surface interferometer (Quartet, Sound & Bright) [37] making it suitable for as-built AM surfaces. It uses a continuous wave laser emitting at 532 nm wavelength and has an average power of 780 mW. This system has an ultrasonic detection bandwidth of 1 - 66 MHz and is capable of detecting out-of-plane ultrasonic displacement. Both the laser ultrasonic generation and detection systems are delivered through an optical fiber. The output from the interferometric detection system is fed into a computer via an oscilloscope (InfiniiVision DSO5014A, Agilent Technologies).

In order to achieve scanning of the two laser beams on the sample surface, the setup uses a galvo mirror (GVS302, Thorlabs) with an optical scan range of ± 20° for the generation laser and a linear stage (M-511.DD1, Physik Instrumente) for the detection laser.

The galvo mirror enables faster scanning due to its lower inertia. The galvo mirror, the linear stage and the oscilloscope are controlled by a computer via a LabVIEW interface for data acquisition. A photodiode (PDA10A2, Thorlabs), placed adjacent to the aperture of the generation laser, captures some of the light from the generation laser, providing a trigger pulse for signal acquisition for the oscilloscope.

The detection system uses a built-in lens (focal depth = 200 mm) to focus the detection beam on the sample. The detection laser spot size at focus was 100 μm diameter, according to the manufacturer specifications. The generation beam is focused into a line using a cylindrical lens (LJ1558RM-C, Thorlabs, focal depth = 300 mm) as shown in Fig. 4. The generation laser line dimensions were 3.69 mm × 1.65 mm (length × width), measured at full width at half maximum (FWHM) intensity. The energy density on the sample surface was calculated to be 4.41 mJ/cm^2, and this is below the ablation threshold for Ti-6Al-4V, which is calculated to be 100 mJ/cm^2 based on [10,38].

Table 3
Laser ultrasonic test parameters used for the experiments.

Instrument	Parameter	Value
Generation laser	Energy per pulse (mJ)	0.268
	Pulse repetition frequency (kHz)	5
	FWHM pulse duration (ns)	23
Oscilloscope	Averaging	64
	Sampling rate (MHz)	50
	Signal length (μs)	20
	Vertical resolution (mV/div)	50

Table 3 lists the parameters used for the experiment.

3.2. Sample and LIPA synthesis

The sample used for the experiments was made of Ti-6Al-4V using the directed energy deposition process, using a plasma arc as the directed energy source. The feedstock was in the form of a wire and was deposited following the single bead deposition strategy with a 1 mm diameter wire [26]. The process is also known as wire-arc additive manufacturing (WAAM) because it uses a wire feed as the feedstock and plasma arc as the energy source. The sample dimensions were 84.5 x 9.3 x 26.4 mm. An SDH of 1.28 mm diameter was drilled on the sample at a depth of 3.7 mm from the scanned surface (inspection surface) as illustrated in Fig. 5. The scan surface was polished to maximise the reflectivity of the surface, thereby improving the signal detection by the interferometric receiver. The one-dimensional (1D) LIPA elements were synthesised (on the sample surface) across the SDH (perpendicular to the axis of the SDH).

The depth of the SDH was chosen to be representative of a depth where the effects of re-melting and re-heating during subsequent layer DED-Arc deposition in the AM process would have subsided. Consequently, the LIPA synthesised was designed for a maximum imaging depth of 5 mm (see Fig. 6). The imaging depth is defined by the -6 dB region of the array sensitivity. A 1D LIPA was constructed by scanning the lasers along one axis of the sample. For the work presented here, the coordinates of generation and detection array element positions are the same. A LIPA of $N = 71$ elements was synthesised and 5041 ($= N^2$) ultrasonic signals were acquired. The separation between the elements (also known as pitch or inter element spacing) was 0.2 mm, resulting in an array aperture of 14 mm. The array sensitivity for the 71 element, 0.2 mm pitch LIPA is shown in Fig. 6 (calculated based on [20]). The pitch was chosen to be less than half the smallest acoustic wavelength being used for imaging (corresponding to 8 MHz) in order to satisfy the Nyquist criterion and ensure that the grating lobes are not produced [39]. For every acquisition, the signals were averaged 64 times. The TFM images are plotted with a pixel size of 0.033 mm x 0.033 mm. Table 4 gives the LIPA and post-processing parameters used in this work.

4. Surface acoustic wave crosstalk suppression

This section details the five different approaches considered for SAW crosstalk suppression: amplitude thresholding (AT); mean waveform subtraction (MWS); principal component subtraction (PCS); frequency-wavenumber filtering ($f - k$ filtering) and phase coherence imaging (PCI).

4.1. Amplitude thresholding

Amplitude thresholding is a simple approach for SAW suppression. This approach considers the fact that in laser ultrasonics, the SAW is usually the wave with the highest amplitude in the detected signal. Thus, the SAW crosstalk in a TFM image can be partially suppressed by applying an amplitude threshold to the raw time-signals prior to

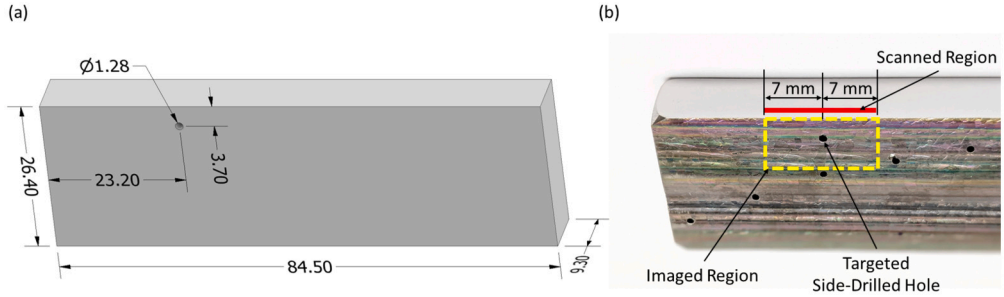

Fig. 5. (a) CAD drawing of the sample used for the experiments showing the sample dimensions and the defect dimensions and location. (b) Close-up photograph of the Ti-6Al-4V DED-Arc sample showing the targeted SDH within the imaged area (dashed yellow rectangle). The 'red' line depicts the scanned aperture size and location of the LIPA.

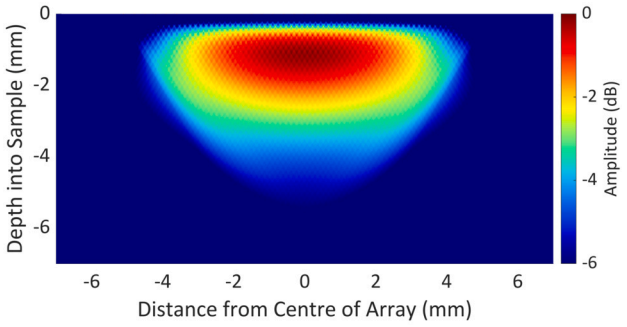

Fig. 6. Sensitivity map for the imaged region based on laser generated and laser detected transverse wave for a LIPA with parameters from Table 4.

Table 4
Parameters used for synthesising LIPA and TFM images.

Method	Parameter	Value
LIPA	Aperture (mm)	14
	Number of elements	71
	Pitch (mm)	0.2
	Number of signals	5041
	Number of sampling points	1000
Digital frequency filtering	Filtering method	Bandpass
	Filter type	Gaussian
	Centre frequency (MHz)	5
	Bandwidth (%)	120
TFM imaging	Wave mode used	Transverse (shear)
	Wave mode velocity (m/s)	3233
	Pixel size (mm x mm)	0.033 x 0.033

image formation. The disadvantage of this technique is that any bulk wave mode signal with an amplitude above the threshold is also suppressed. For this reason, the threshold is evaluated based on the peak amplitude of each individual signal: for every ultrasonic signal, there is a corresponding threshold value rather than a global threshold. This approach considers the variability across the ultrasonic signals, making it unbiased. The threshold level was finally optimised based on the Signal-to-Crosstalk Ratio (see section 5) of the resulting TFM image. For the work presented here, the optimum threshold was 10% of the peak amplitude of the SAW in each ultrasonic signal.

$$S_{TR}(t_{TR}(\mathbf{r})) = \begin{cases} sign(S_{TR}(t_{TR}(\mathbf{r})))A_{thresh} & \text{if } |S_{TR}(t_{TR}(\mathbf{r}))| \geq A_{thresh} \\ S_{TR}(t_{TR}(\mathbf{r})) & \text{otherwise} \end{cases} \tag{7}$$

where $A_{thresh} = 0.1 \times max(S_{TR}(t_{TR}(\mathbf{r})))$

Fig. 7 (b) illustrates the implementation of the amplitude thresholding on a representative LU signal (Fig. 7 (a)).

4.2. Mean waveform subtraction

Mean waveform subtraction for SAW suppression is based on subtracting the SAW response from each signal according to the separation distance between generation and detection of LIPA elements. The application of the method to LIPAs is described below.

Firstly, the ultrasonic signals of the FMC are grouped according to the separation distance between generation and detection of LIPA elements. The LIPA synthesised in this work is a periodic array (i.e. constant element pitch). Following [40], we introduce the parameter Δ, which describes the integer multiple of the array pitch that equals the surface separation for a given ultrasonic signal. In this case, the ultrasonic signals are taken in groups with the same value of Δ (see Fig. 8). These are elements of the diagonals of the full matrix with the same offset from the main diagonal.

The group of ultrasonic signals for which $\Delta = 0$ corresponds to the main diagonal of the full matrix and also forms a group in this analysis. The SAW will have the same time-of-arrival for all ultrasonic signals in the same group, since the surface path length between the generation and the detection element is the same and the SAW velocity is constant for the material investigated here. Several other types of signal will also show consistent time-of-arrival in all ultrasonic signals with a constant Δ, such as bulk reflections from a flat back-wall and any other mode of surface-propagating wave. A 'mean waveform', $\overline{S_\Delta}$, for each group of signals can be obtained by taking the mean amplitude of all the ultrasonic signals in this group at each point in time, as shown in the following equation:

$$\overline{S_\Delta}(t) = \frac{1}{N_\Delta} \sum_{\Delta} S_{TR}(t) \tag{8}$$

where N_Δ is the number of signals in the FMC dataset with the same separation distance Δ between generation and detection elements. This mean waveform is then subtracted from each of the ultrasonic signals with the corresponding Δ value to achieve SAW suppression:

$$s_{TR} = S_{TR} - \overline{S_\Delta}(t) \tag{9}$$

Fig. 7 (c) illustrates the implementation of the mean waveform subtraction on a representative LU signal (Fig. 7 (a)).

4.3. Principal component subtraction

Even though SAWs that are temporally coherent across all captured ultrasonic signals will be represented in the mean waveform and will be subtracted from the raw signals, each ultrasonic signal in the groups of the same Δ is likely to feature some residual content from the direct SAW signal due to slight variations in the amplitude and time-of-arrival of the SAW (Fig. 7 (c)). After mean waveform subtraction, the residual SAW signal content in the ultrasonic signal batch, will be associated with the times in the original, raw ultrasonic signal groups of Δ that featured the highest variance in amplitude values (since variance describes

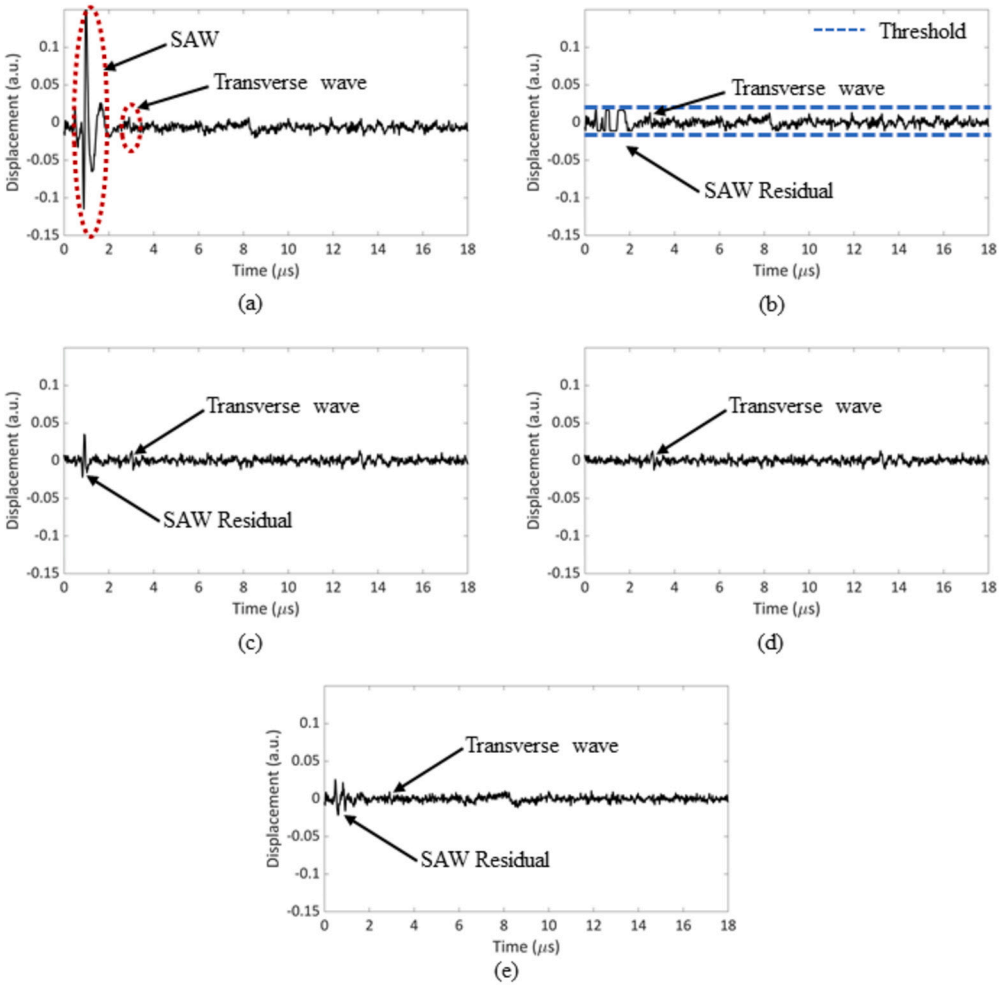

Fig. 7. Plots of the same laser ultrasonic signal showing the transverse wave echo originating from a defect present at 4 mm depth and the SAW: (a) before SAW suppression; (b) after amplitude thresholding; (c) after mean waveform subtraction; (d) after principal component subtraction; (e) after frequency-wavenumber filtering.

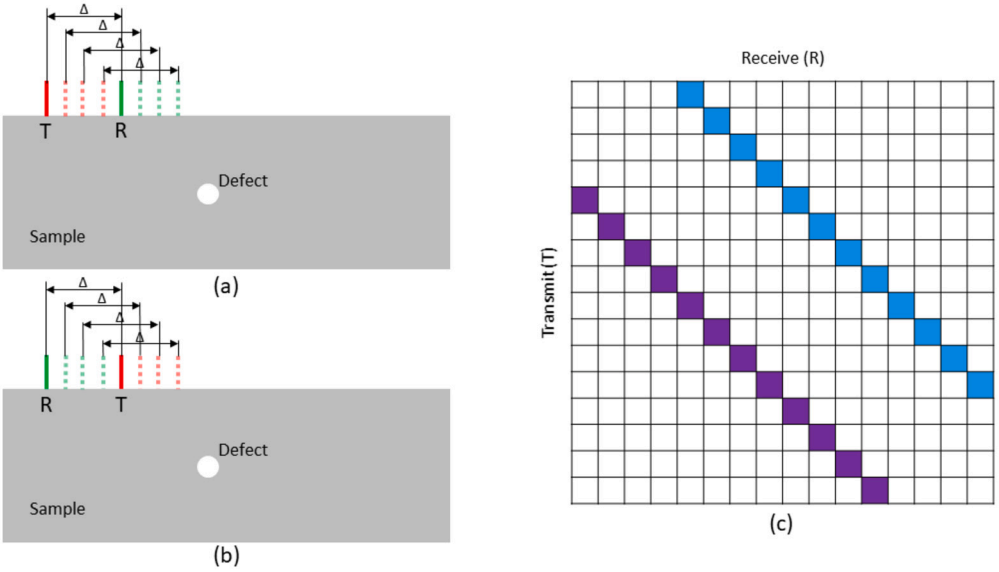

Fig. 8. (a) Schematic showing a batch of transmit (T) - receive (R) scanning positions (element pairs) with the same spacing (Δ). (b) Schematic showing a batch of transmit (T) - receive (R) pairs in swapped positions (i.e., R - T) with the same spacing (Δ) with respect to (a). (c) Representation of the full matrix for the LIPA shown in (a) and (b). The 'blue' diagonal corresponds to the ultrasonic signals for the batch of T - R shown in (a) and the 'purple' diagonal corresponds to the ultrasonic signals with swapped T and R positions (i.e., R - T) shown in (b).

the square of average squared deviation from the mean). These residual SAW contributions can be suppressed further by the subtraction of appropriately weighted principal components, obtained by covariance analysis of the amplitude values measured at each time across each ultrasonic signal group of the same Δ [40,41]. Principal component analysis (PCA) is thus performed on groups of ultrasonic signals, giving the principal components of each grouping of signals as eigenvectors of a covariance matrix. Finally, the principal components with the largest eigenvectors, which include the SAW, are subtracted from each acquired ultrasonic signal, resulting in SAW suppression. This process is described in detail in Couret & Paul [40] for FMC data acquired with transducer-based ultrasonic phased arrays.

The ultrasonic signals for each Δ are organised in a matrix A_Δ with number of rows equal to $2(N-\Delta)$ and number of columns equal to m, where m is the number of sampling points. The covariance matrix C_Δ associated with this data set is then calculated, which has dimensions $m \times m$, and is populated by the variances and covariances of the amplitude values measured at each time across this group of ultrasonic signals. The mean waveform subtracted ultrasonic signals, s_{TR}, can be expressed in the eigen basis, $v_{\Delta,k}$ as:

$$s_{TR}(t) = \sum_{k=1}^{m} \left(\sum_{l=1}^{m} s_{TR}(l) v_{\Delta,k}(l) \right) v_{\Delta,k}(t) \tag{10}$$

These eigenvectors are then ranked according to their associated eigenvalues, with the eigenvector possessing the highest associated eigenvalue being the *first principal component* and so on for the second highest eigenvalue. Each principal component can likewise be plotted as a shape function with the same number of sampling points as an ultrasonic signal (m points). These shape functions will resemble various parts of the residual direct SAW signal persisting in the ultrasonic signals after mean waveform subtraction, and can hence be used to achieve further SAW suppression by subtraction, after appropriate scaling. Depending on the temporal resolution and capture duration of the ultrasonic signals recorded during full matrix capture, m can be a very large number (e.g. several thousand), and m principal components are obtained as eigenvectors of the $m \times m$ covariance matrix. Since the first principal component represents the majority of the variance around the mean waveform, with subsequent principal components capturing less and less, subtracting higher order principal components from the zero-mean ultrasonic signals yields diminishing returns in SAW suppression. A threshold in the number of principal components to subtract can therefore be set to improve computational efficiency. Following [40], an adaptation of the Kaiser rule can be used to calculate a threshold value against which the eigenvalues of the eigenvectors are compared. Eigenvectors with eigenvalues that fall below this threshold are not included in the scaling and subtraction stage. In this case, equation (10) becomes:

$$s_{TR}^{p} = \sum_{k=1}^{K_\Delta} \left(\sum_{l=1}^{m} s_{TR}(l) v_{\Delta,k}(l) \right) v_{\Delta,k}(t) \tag{11}$$

where s_{TR}^{p} is the matrix containing the first few principal components representing the coherent SAW signals and K_Δ is the integer representing the best number of principal components that represent the coherent SAW signal. Following this step, the SAW suppressed FMC ultrasonic signals s_{TR}^{*} are given from the following expression:

$$s_{TR}^{*} = s_{TR} - s_{TR}^{p} \tag{12}$$

Fig. 7 (d) illustrates the implementation of the principal component subtraction on a representative LU signal (Fig. 7 (a)).

4.4. Frequency-wavenumber filtering

In a non-dispersive medium, the ultrasonic wave modes travel with a unique but constant velocity. This unique velocity feature opens up a way for filtering the wave modes using their velocity. This is achieved by transforming the ultrasonic signals into the frequency-wavenumber ($f-k$) domain where the slope of the $f-k$ domain gives the velocity of the propagating wave mode [42]. However, this is only true for guided waves (such as SAW and Lamb waves) and it is not true for bulk wave modes, as bulk waves do not propagate parallel to the array. Hence, the SAW mode can be filtered in the $f-k$ domain using its velocity. Transformation to the $f-k$ domain requires spatially sampled data which is readily available from the FMC. In LIPA FMC acquisition, each row (one row of FMC represents data from all receiving elements corresponding to one transmission element, Fig. 9(a)) of the full matrix provides the spatially sampled data to perform a two-dimensional fast Fourier transform (2D FFT) to obtain the frequency-wavenumber spectrum of the data. SAW suppression is performed by creating a band-stop filter in the $f-k$ domain and multiplying the filter with the $f-k$ data. The graphic representation of this process is shown in Fig. 9. The size of the $f-k$ filter used is the same as that of the $f-k$ data, for compatibility.

The $f-k$ filtering process for 1D wave propagation (in x-direction) can be mathematically expressed as [43]:

$$U_W(f,k_x) = U(f,k_x) W(f,k_x) \tag{13}$$

where $U(f,k_x)$ is the $f-k$ spectrum of each row of the FMC, $W(f,k_x)$ is the 2D $f-k$ filter function and $U_W(f,k_x)$ is the filtered spectrum.

In this work, a 1D band-stop filter was constructed for every k_x. Then the 2D band-stop filter was created from all 1D filters for all k_x. In order to construct the 1D band-stop filters, the gradient (velocity) of the forward-travelling SAW (v_{SAW}) was extracted from the $f-k$ data. This gradient allows the frequency corresponding to the absolute amplitude peak of the forward-travelling SAW ($f_{\mathrm{SAW+}}$) for each k_x to be calculated according to:

$$f_{\mathrm{SAW+}}(k_x) = \frac{v_{\mathrm{SAW}} k_x}{2\pi} \tag{14}$$

For every k_x, a 1D Gaussian band-stop filter was created according to the equation:

$$w_{k,\mathrm{SAW+}}(f) = 1 - \frac{\exp(-(f - f_{\mathrm{SAW+},k})^2)}{2\sigma_{\mathrm{BS}}^2} \tag{15}$$

Where σ_{BS} is the standard deviation of the Gaussian band-stop filter. In this work, the value of σ_{BS} was evaluated based on the full width at half maximum (w_{FWHM}) of the SAW amplitude peak according to:

$$\sigma_{\mathrm{BS}} = A \frac{w_{\mathrm{FWHM}}}{2.355} \tag{16}$$

A scaling factor (A) was used to increase the standard deviation value to achieve SAW filtering without filter artefacts. A value of $A = 10$ was used in the experimental results presented in this paper. Equivalent 1D filters ($w_{k,\mathrm{SAW-}}(f)$) were designed for the backward-travelling SAWs, centred at $f_{\mathrm{SAW-}}$.

Two 2D filters were created, one for the forward ($w_{\mathrm{SAW+}}(f,k)$) and one for the backward ($w_{\mathrm{SAW-}}(f,k)$) travelling SAWs, for every k_x. The two filters were combined to produce a single 2D filter, $W(f,k_x)$ according to the following equation:

$$W(f,k_x) = \begin{cases} w_{\mathrm{SAW+}}(f,k_x) & \text{if } w_{\mathrm{SAW+}}(f,k_x) \le w_{\mathrm{SAW-}}(f,k_x) \\ w_{\mathrm{SAW-}}(f,k_x) & \text{if } w_{\mathrm{SAW+}}(f,k_x) > w_{\mathrm{SAW-}}(f,k_x) \end{cases} \tag{17}$$

This 2D filter was applied to the real and imaginary parts of the Fourier spectrum separately as described in equation (13). Following this step, the filtered spectrum $U_W(f,k_x)$ was transformed back into the time-space domain using the inverse 2D FFT in order to obtain the filtered wavefield $u_W(t,x)$:

$$u_W(t,x) = {F_{2D}}^{-1}[U_W(f,k_x)] \tag{18}$$

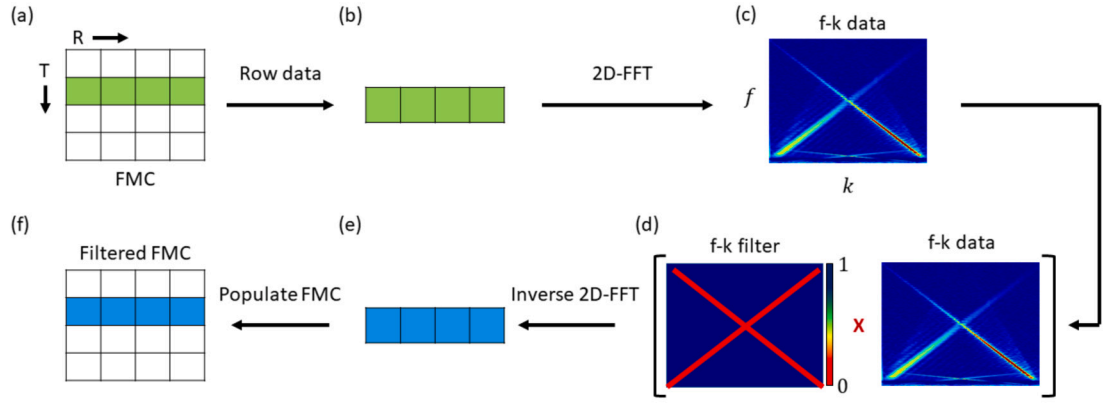

Fig. 9. (a) - (f) Schematic of the $f-k$ filtering process.

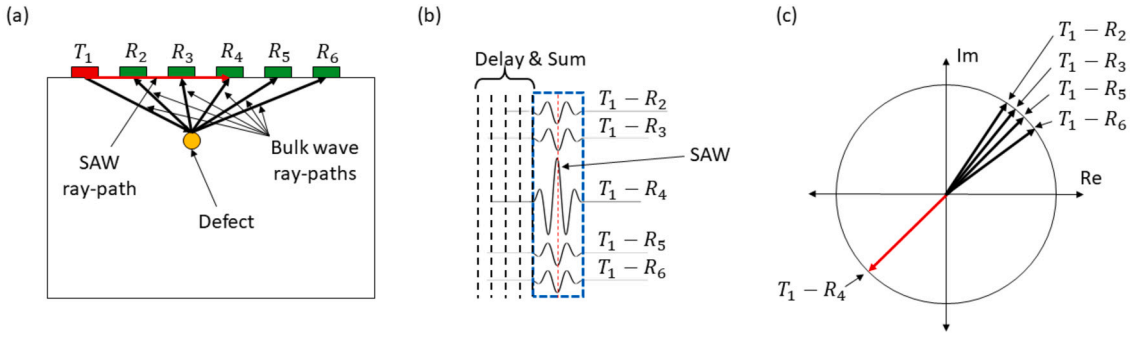

Fig. 10. Simplified, schematic representation of phase coherence in the received ultrasonic signals. (a) Cross-sectional view of a sample with a defect and a 6-element 1D LIPA synthesised on its top surface. T_1 is the transmitting element and R_2 to R_6 are the receiving elements. (b) TFM implementation on the 'pixel' representing the defect (in (a)) showing the SAW crosstalk from the T_1-R_4 element combination. (c) Plot representation of the phase of the signals (in (b)) for a specific sampling point (red dotted line in (b)).

This process (equations (13) & (18)) was repeated for each row of the FMC, prior to forming a TFM image using equation (1). Fig. 7 (e) illustrates the implementation of the $f-k$ filtering process on a representative LU signal (Fig. 7 (a)).

4.5. Phase coherence imaging

Phase coherence imaging is an adaptive beamforming algorithm that enhances the ultrasonic image at pixels where there is strong spatial coherence in the raw data [44]. The phase of every ultrasonic signal is measured and high phase coherence between signals is observed when the synthetic focal point is at an internal feature because the signals are all scattered from the same point. Conversely, the surface wave signals causing crosstalk travel directly from the location of the ultrasonic generation array element to the location of the ultrasonic detection array element, without scattering from points in the bulk material. Hence there is low phase coherence of surface wave signals in the raw data at image pixels in the bulk material (see relevant discussion in section 2.2 and Fig. 10).

In phase coherence imaging, a weighting factor is applied to each individual pixel of the original TFM ultrasonic image in order to reduce the effects of signals that are not spatially coherent (e.g. noise, grating lobe signals or SAW). By calculating the phase coherence of the signals at each pixel and applying the coherence weighting factor, the pixels containing only SAW crosstalk are suppressed, while the pixels containing bulk wave information are preserved.

A variety of methodologies have been published for measuring the coherence of ultrasonic signals [45]. The circular coherence factor (CCF) and the vector coherence factor (VCF) have been presented as the best performing phase coherence factors, from these published methods, with the latter offering a less computationally demanding algorithm.

The vector coherence factor, $V(\mathbf{r})$, is used in the work presented in this paper and is calculated by the following equation [45]:

$$V(\mathbf{r}) = \sqrt{\left(\sum_{T=1}^{N}\sum_{R=1}^{N}\frac{Re(S_{TR}(t_{TR}(\mathbf{r})))}{|S_{TR}(t_{TR}(\mathbf{r}))|}\right)^2 + \left(\sum_{T=1}^{N}\sum_{R=1}^{N}\frac{Im(S_{TR}(t_{TR}(\mathbf{r})))}{|S_{TR}(t_{TR}(\mathbf{r}))|}\right)^2} \tag{19}$$

The final image is then produced by taking the product of the TFM image, $I(\mathbf{r})$, and the vector coherence factor, $V(\mathbf{r})$.

$$I_{VCF}(\mathbf{r}) = I(\mathbf{r})\,V(\mathbf{r}) \tag{20}$$

5. Results and discussion

The acquired data was processed using a computer with an Intel(R) Core(TM) i7-4770K CPU @ 3.50 GHz processor, 4 cores and 32 GB RAM. The computer's GPU was not used during the data and image processing. All TFM images presented in this section are plotted with a dynamic range varying from 0 dB to the RMS noise level, wherein the RMS noise level is measured outside the crosstalk region for every image (i.e. in a crosstalk and defect free area). The TFM images are plotted showing the noise floor in order to compare the effectiveness of the methods. A new parameter, signal-to-crosstalk ratio (SCR) is introduced in this paper and this parameter is used to assess the performance of the suppression techniques used. The evaluation of SCR is described using Fig. 11 (a). In Fig. 11 (a), the region inside the dotted black triangle is an approximation of the SAW crosstalk region. SCR is given by the ratio of peak intensity in the region of the defect (the black dotted circle region in Fig. 11 (a)) and the RMS value of the triangular region.

Fig. 11 (a) shows the normalised TFM image using transverse wave mode obtained from the FMC data. The image was normalised with

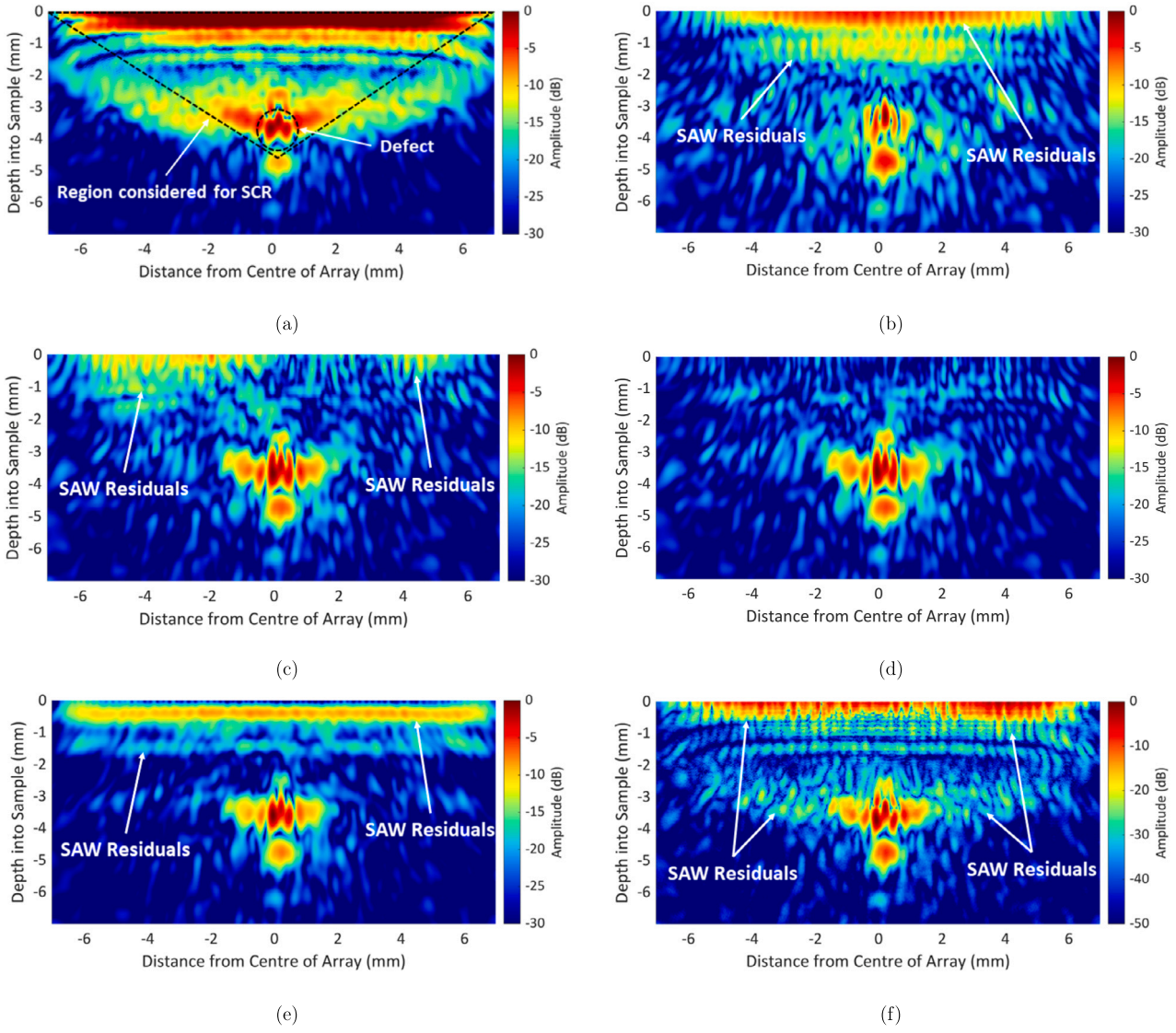

Fig. 11. TFM ultrasonic images using transverse wave arrival and a 5 MHz digital filter: (a) without SAW suppression, (b) after amplitude thresholding, (c) after mean waveform subtraction, (d) after principal component subtraction, (e) after frequency-wavenumber filtering, (f) after phase coherence imaging.

respect to the defect (maximum intensity within the region inside the black dotted circle in Fig. 11 (a)) using equation (3). It is observed that the SAW artefact and crosstalk region are present up to a depth of 4.3 mm from the scan surface. Hence, the defect indication from the transverse wave arrival in this TFM image is affected by it. The SCR of the TFM image was measured as 6.97 dB.

Fig. 11 (b)-(f) show the TFM images generated after the various methods for SAW suppression presented in section 4 having been applied and Table 5 presents the comparison of the performance of each method with respect to the SCR and processing time required to generate each TFM image. The quantitative results presented in the top half of Table 5 demonstrate that all methods perform very well at suppressing the SAW crosstalk and improve SCR by at least 8.5 dB and at most 16 dB.

According to this SCR comparison, the amplitude threshold method achieves the lowest improvement in SCR, while PCS achieves the highest improvement in SCR. It is to be noted that even though PCI is used as a SAW suppression technique, the parameter SCR cannot be used to compare the performance of PCI with the other techniques. This is because PCI is a nonlinear imaging process and this is evidenced by the difference in dynamic ranges used in the TFM images presented in Fig. 11. Therefore comparing the SCR improvement of PCI with the other techniques would be meaningless. The quantitative improvement in SCR due to PCI is not included in the top half of table.

Table 5
Summary of performance comparison of various SAW crosstalk suppression techniques.

Suppression method	SCR (in dB)	Change in processing time (%)
No suppression	6.97	Baseline
AT	15.45	1
$f-k$ filtering	17.58	33
MWS	18.95	27
PCS	22.78	27
	SCR* (in dB)	
PCI	22.94	46
AT + PCI	24.32	48
$f-k$ filtering + PCI	35.04	73
MWS + PCI	35.52	60
PCS + PCI	36.44	67

SCR*: The PCI operation is nonlinear and hence affects the signal and crosstalk nonlinearly.

The PCI method can be combined with other methods for effective SAW suppression. Fig. 12 shows the TFM images wherein the other SAW

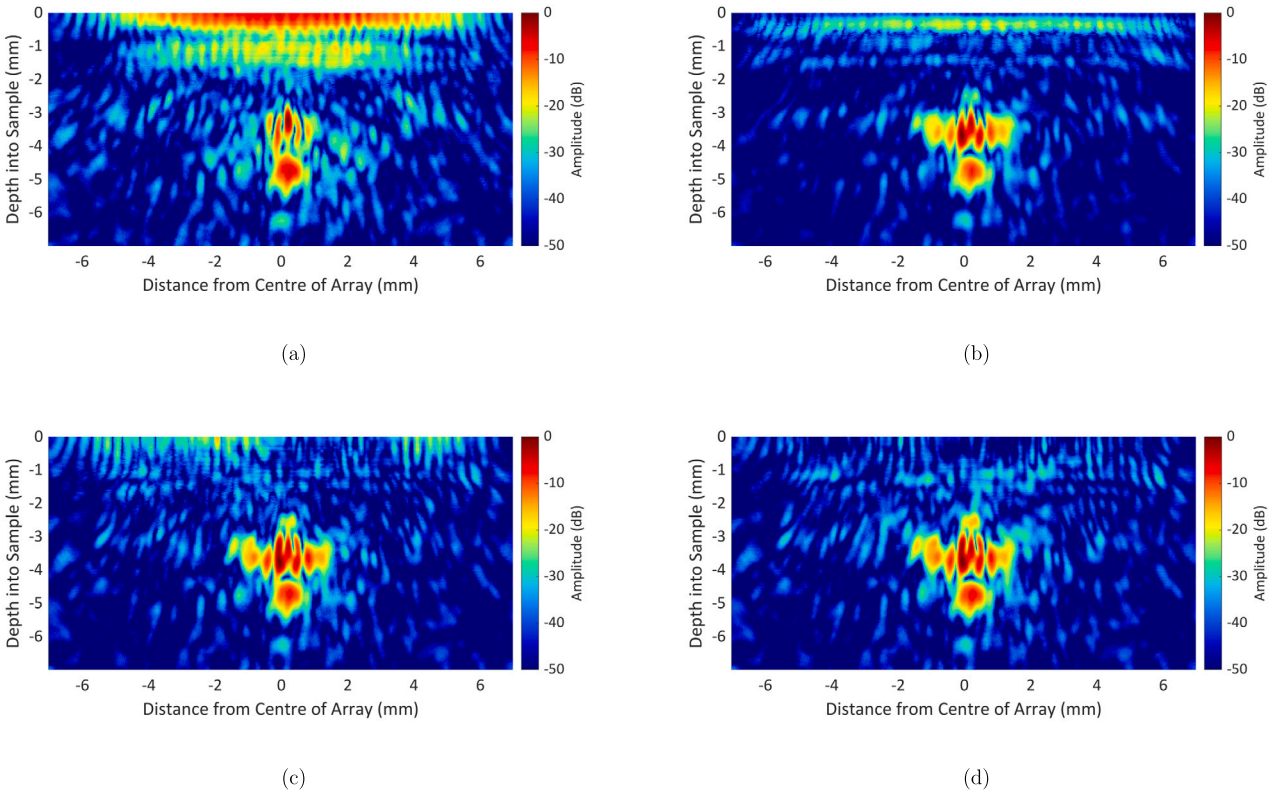

Fig. 12. TFM ultrasonic images obtained by implementing PCI after (a) amplitude thresholding, (b) $f-k$ filtering, (c) mean waveform subtraction, (d) principal component subtraction.

suppression methods are combined with the PCI method. It is observed that the PCS followed by PCI gives the best SCR of 36.44 dB compared to the SCR of 22.94 dB by using PCI alone.

Regarding the methods that perform best at increasing SCR, the qualitative comparison of the TFM images presented in Fig. 11 shows that PCS achieves the best SAW suppression, where the SAW has successfully been suppressed throughout the SAW affected crosstalk region (Fig. 11 (d)). Regarding the TFM image with the amplitude threshold at 10% of the SAW amplitude (Fig. 11 (b)) and comparing it with those resulting from other methods (Fig. 11 (c-f)), it can be seen that some signal from the defect (signal with lowest amplitude from left and right part of the defect) has been suppressed along with the SAW induced crosstalk. Fig. 11 (c) shows the TFM image generated after mean wave subtraction. It can be observed that SAW residuals remain (close to the scan surface) after this method has been applied. These residuals have been effectively removed when using the PCS method (Fig. 11 (d)), which follows the MWS method, as described in section 4.

Table 5 includes the comparison between processing time required for each TFM image shown in Fig. 11 and Fig. 12. It shows that amplitude threshold is the technique that requires the least amount of computational resources while PCI and $f-k$ filtering are more demanding. PCI takes approximately 46% more processing time than the other methods and this is expected as it is an image processing method, whereas the other methods are signal processing approaches. $f-k$ filtering takes approximately 33% more processing time than the other methods. This method is computationally expensive for either an array with large number of elements or large number of sampling points or both. This is because $f-k$ filtering involves computing the 2D FFT; as a result, the computation time increases as the size of the 2D FMC matrix increases.

All presented methods perform very well at suppressing the SAW crosstalk. The following part of this section discusses advantages and disadvantages of presented methods, in addition to those previously presented, in order to aid the choice of the most appropriate one depending on the inspection requirements.

The AT method is comparatively a simple approach. The computational resource required for this method is relatively low since it only involves simple mathematical operations. This method is effective when the wave mode to be suppressed is an order of magnitude higher than the wave mode to be retained. Hence in the case of LU, this method works only to suppress SAW and its strong reflections. This method cannot be used to suppress other, low amplitude modes such as surface skimming longitudinal wave and the airborne shock wave (arising from ablative generation). Furthermore, this method is effective when SAW induced artefacts are present in the TFM image but suppresses part of the bulk wave as well as the SAW when SAW crosstalk takes place (see Fig. 11 (b)), which is the experimental case presented here. The effectiveness of this method highly depends on the threshold value chosen, which, in this work, is 10% of the peak amplitude of the SAW.

The MWS method, applied on its own, is a relatively simple technique as it involves basic mathematical operations. This method will suppress the direct wave arrival from all surface-propagating waves (SAW, surface-skimming longitudinal wave, shock wave etc.), as well as other temporally coherent features such as bulk wave echoes from a flat back-wall, parallel to the scanned surface. The disadvantage of this method is that it becomes less effective when there is a variation in the amplitudes of the wave modes to be suppressed. The variation in amplitudes may arise due to: 1) variation in the optical energy output from the ultrasonic generation laser; 2) variation in the laser spot size and subsequent laser energy density due to changes in the focusing of the laser beam; and 3) changes in surface quality due to roughness or different material (e.g. local presence of metal oxides).

The PCS method is an effective method for suppressing the wave modes propagating on the scan surface and can effectively suppress any residuals left after MWS as seen in Fig. 11 (d). This method preserves the bulk wave mode when SAW crosstalk takes place. The main challenge in implementing the PCS method is in choosing the best number of

principal components for extracting the SAW wave mode. In the case of LIPAs, SAW suppression using PCS is easier to work with since the SAW wave mode has the highest energy of the wave modes generated in LU and hence the first few principal components of the re-arranged (descending) eigenvalues.

The $f-k$ filtering is a highly effective technique in crosstalk suppression as it targets a specific wave mode based on its velocity. The $f-k$ filtering can be used to suppress any wave mode whose dispersion curves can be measured. Hence, this method can also be applied for wave suppression in dispersive media. This is a unique advantage of this method compared to the others used in this work. In addition to SAW suppression, this method can be used to suppress shock waves and reflected SAWs. The design of the filter used is critical and a poor filter design can introduce new artefacts. This method also requires sufficient spatial sampling to resolve the different wavelengths.

Combining the above methods with PCI was also found to be very effective for SAW suppression. However, this approach comes at the cost of an increase in processing time, which may or may not be an issue depending on the available computational resources. It is noted here that PCI will also achieve suppression of multi-modal artefacts induced by other wave modes including bulk wave modes. This is because the contribution of other, unimaged wave modes will not exhibit phase coherence as they are out-of-focus at the imaged wave velocity and thus, PCI will suppress them.

The depth of the SDH was chosen to be representative of a depth where the effects of re-melting and re-heating during subsequent layer DED-Arc deposition in the AM process would have subsided. Defects appearing closer to the surface would be subjected to cyclic change due to melting, heating and cooling caused by the AM process as described in section 1. However, the presented SAW subtraction techniques will have applications beyond in-process AM inspection and for this reason we note that the proposed methods would be effective at suppressing the SAW from defects located nearer to the surface than the case presented here, as the depth of the defect was chosen to be at a worst-case scenario with respect to the SAW crosstalk effect (see relevant discussion in section 2.2). A limitation is when the defect is very close to the surface, closer than 1 mm for the LIPA characteristics presented in Table 4 (see Fig. 11 (a)). This is because, at this depth, the SAW summed by the TFM algorithm using the transverse wave velocity will be coherent (see relevant discussion in section 2.2). In this case (defect depth <1 mm), some of the methods (AT, MWS, f-k filtering) would be less effective in SAW suppression than others (see Fig. 11 (b), (c), (e), (f)). PCA is expected to cope better at these depths, as it is the most successful method at suppressing the SAW at the surface as shown in Fig. 11 (d).

The SAW suppression methods presented in this paper have been applied for the case of imaging using TFM. However, SAW induced artefacts and crosstalk are present in other imaging algorithms when laser ultrasound data are used, for example, B-scan [12], SAFT [46] or plane wave imaging [47]. All the presented methods can be used with these imaging algorithms to improve imaging quality. An exception to this is PCI, which can only be used with imaging algorithms that perform focusing and this is not the case, for example, with B-scan.

6. Conclusions

In AM process, near-surface defects beyond the re-melting and re-heating zones in the build should be imaged for successful, in-process NDE. Ultrasonic bulk wave imaging using LIPAs can detect near-surface defects that cannot be imaged using SAWs, without couplant and remotely. However, the presence of SAW crosstalk in bulk wave imaging hinders the successful imaging of near-surface defects. Thus, SAW crosstalk suppression is essential.

We presented five different methods for SAW crosstalk suppression and demonstrated their effectiveness in imaging a 1.28 mm SDH, located at 3.7 mm below the scanned surface, using LIPAs, in a Ti-6Al-4V DED-Arc made sample. All presented methods perform very well at suppressing the SAW crosstalk. The AT method was shown to be less effective in the case of a SAW crosstalk but can be applied to suppress SAW induced artefacts. All other methods can be implemented for both these cases. PCS has been shown to be best at suppressing the SAW while preserving the bulk wave signal. PCI is an image processing method whereas the other methods are signal processing approaches and hence PCI can be combined with other methods to maximise SAW crosstalk suppression as well as suppression of multi-modal artefacts induced by other wave modes, including bulk wave modes. However, PCI requires more computational resources and processing time. It is noted here that the processing time of all these methods can be reduced to <1 second if a GPU is used during the post-processing [48]. In this case, successful SAW suppression can be achieved in real-time, during the AM cycle, for in-process inspection.

The focus of this paper has been on SAW suppression for the purpose of defect detection in AM components. One future aim is to develop methods for defect characterisation, such as size and type (e.g. porosity or lack of fusion) of defect in order to link them with the AM deposition process. Another future aim is to evaluate these methods with defects naturally occurring in AM as opposed to idealised ones (side drilled holes) and ultimately test the performance during AM deposition.

CRediT authorship contribution statement

Geo Davis: Conceptualization, Methodology (AT, $f-k$ filtering, and PCS), Investigation, Validation, Formal analysis, Writing – Original draft & review. **Theodosia Stratoudaki:** Conceptualization, Formal analysis, Writing – original draft & review, Supervision, Funding acquisition. **Peter Lukacs:** Methodology (PCI), Software, Formal analysis, Writing – original draft & review (PCI). **Matthew W. Riding:** Methodology ($f-k$ filtering, MWS and PCS), Writing – original draft ($f-k$ filtering, MWS and PCS). **Ahmed Al Fuwaires:** Methodology ($f-k$ filtering, PCS). **Panagiotis Kamintzis:** Investigation. **Don Pieris:** Investigation. **Alan Keenan:** Methodology (AT). **Paul Wilcox:** Methodology (MWS), Writing – review & editing. **Gareth Pierce:** Resources, Writing – review & editing, Funding acquisition. **Charles MacLeod:** Resources, Writing – review & editing, Funding acquisition. **Stewart Williams:** Resources, Writing – review & editing, Funding acquisition.

Declaration of competing interest

The authors declare that they have no known competing financial interests or personal relationships that could have appeared to influence the work reported in this paper.

Data availability

All data underpinning this publication are openly available from the University of Strathclyde KnowledgeBase at https://doi.org/10.15129/0cfd48c9-733d-4636-8f0a-b28bf48a34bd.

Acknowledgements

This work was supported by the UK Engineering and Physical Sciences Research Council [EP/T012862/1, EP/R513349/1, EP/V051814/1, EP/S023275/1, EP/S023879/1, EP/R027218/1]. The authors wish to acknowledge Nicolas Paul from EDF, France, for his support with the mean waveform subtraction and principal component subtraction techniques.

References

[1] R. Russell, D. Wells, J. Waller, B. Poorganji, E. Ott, T. Nakagawa, H. Sandoval, N. Shamsaei, M. Seifi, Qualification and certification of metal additive manufactured hardware for aerospace applications, in: Additive Manufacturing for the Aerospace Industry, 2019, pp. 33–66.

[2] S.A. Tofail, E.P. Koumoulos, A. Bandyopadhyay, S. Bose, L. O'Donoghue, C. Charitidis, Additive manufacturing: scientific and technological challenges, market uptake and opportunities, Mater. Today 21 (1) (2018) 22–37.
[3] J.C. Najmon, S. Raeisi, A. Tovar, Review of additive manufacturing technologies and applications in the aerospace industry, in: Additive Manufacturing for the Aerospace Industry, 2019, pp. 7–31.
[4] B. Blakey-Milner, P. Gradl, G. Snedden, M. Brooks, J. Pitot, E. Lopez, M. Leary, F. Berto, A. du Plessis, Metal additive manufacturing in aerospace: a review, Mater. Des. 209 (2021) 110008.
[5] A. Gisario, M. Kazarian, F. Martina, M. Mehrpouya, Metal additive manufacturing in the commercial aviation industry: a review, J. Manuf. Syst. 53 (2019) 124–149.
[6] S.K. Everton, M. Hirsch, P. Stravroulakis, R.K. Leach, A.T. Clare, Review of in-situ process monitoring and in-situ metrology for metal additive manufacturing, Mater. Des. 95 (2016) 431–445.
[7] Y. Javadi, N.E. Sweeney, E. Mohseni, C.N. MacLeod, D. Lines, M. Vasilev, Z. Qiu, R.K. Vithanage, C. Mineo, T. Stratoudaki, et al., In-process calibration of a non-destructive testing system used for in-process inspection of multi-pass welding, Mater. Des. 195 (2020) 108981.
[8] R. Zimermann, E. Mohseni, D. Lines, R.K. Vithanage, C.N. MacLeod, S.G. Pierce, A. Gachagan, Y. Javadi, S. Williams, J. Ding, Multi-layer ultrasonic imaging of as-built wire+ arc additive manufactured components, Addit. Manuf. 48 (2021) 102398.
[9] A. Lopez, R. Bacelar, I. Pires, T.G. Santos, J.P. Sousa, L. Quintino, Non-destructive testing application of radiography and ultrasound for wire and arc additive manufacturing, Addit. Manuf. 21 (2018) 298–306.
[10] C.B. Scruby, L.E. Drain, Laser Ultrasonics, Techniques and Applications, Adam Hilger, Bristol, UK, 1990.
[11] J.P. Monchalin, Optical detection of ultrasound, IEEE Trans. Ultrason. Ferroelectr. Freq. Control 33 (5) (1986) 485–499.
[12] D. Cerniglia, M. Scafidi, A. Pantano, J. Rudlin, Inspection of additive-manufactured layered components, Ultrasonics 62 (2015) 292–298.
[13] P. Dryburgh, D. Pieris, F. Martina, R. Patel, S. Sharples, W. Li, A.T. Clare, S. Williams, R.J. Smith, Spatially resolved acoustic spectroscopy for integrity assessment in wire–arc additive manufacturing, Addit. Manuf. 28 (2019) 236–251.
[14] R.J. Smith, W. Li, J. Coulson, M. Clark, M.G. Somekh, S.D. Sharples, Spatially resolved acoustic spectroscopy for rapid imaging of material microstructure and grain orientation, Meas. Sci. Technol. 25 (5) (2014) 055902.
[15] R.J. Smith, M. Hirsch, R. Patel, W. Li, A.T. Clare, S.D. Sharples, Spatially resolved acoustic spectroscopy for selective laser melting, J. Mater. Process. Technol. 236 (2016) 93–102.
[16] D. Lévesque, C. Bescond, M. Lord, X. Cao, P. Wanjara, J.-P. Monchalin, Inspection of additive manufactured parts using laser ultrasonics, in: AIP Conference Proceedings, vol. 1706, AIP Publishing LLC, 2016, p. 130003.
[17] D. Lévesque, C. Bescond, C. Cojocaru, Laser-ultrasonic inspection of cold spray additive manufacturing components, in: AIP Conference Proceedings, vol. 2102, AIP Publishing LLC, 2019, p. 020026.
[18] Y. Zeng, X. Wang, X. Qin, L. Hua, G. Liu, S. Guan, Laser ultrasonic inspection of defects in wire arc additive manufactured samples with different surface profiles, Measurement 188 (2022) 110597.
[19] G. Davis, R. Nagarajah, S. Palanisamy, R.A.R. Rashid, P. Rajagopal, K. Balasubramaniam, Laser ultrasonic inspection of additive manufactured components, Int. J. Adv. Manuf. Technol. 102 (2019) 2571–2579.
[20] T. Stratoudaki, M. Clark, P.D. Wilcox, Laser induced ultrasonic phased array using full matrix capture data acquisition and total focusing method, Opt. Express 24 (19) (2016) 21921–21938.
[21] P. Lukacs, G. Davis, T. Stratoudaki, Y. Javadi, G. Pierce, A. Gachagan, Remote, volumetric ultrasonic imaging of defects using two-dimensional laser induced phased arrays, in: Quantitative Nondestructive Evaluation, vol. 85529, American Society of Mechanical Engineers, 2021, V001T18A001.
[22] D. Pieris, T. Stratoudaki, Y. Javadi, P. Lukacs, S. Catchpole-Smith, P.D. Wilcox, A. Clare, M. Clark, Laser induced phased arrays (LIPA) to detect nested features in additively manufactured components, Mater. Des. 187 (2020) 108412.
[23] P. Lukacs, T. Stratoudaki, G. Davis, A. Gachagan, Adaptive data acquisition for fast ultrasonic imaging using laser induced phased arrays, in: Quantitative Nondestructive Evaluation, vol. 85529, American Society of Mechanical Engineers, 2021, V001T18A003.
[24] P. Lukacs, G. Davis, D. Pieris, A. Gachagan, T. Stratoudaki, Grating lobe suppression through novel, sparse laser induced phased array design, in: 2022 IEEE International Ultrasonics Symposium (IUS), IEEE, 2022, pp. 1–4.
[25] C. Holmes, B.W. Drinkwater, P.D. Wilcox, Post-processing of the full matrix of ultrasonic transmit–receive array data for non-destructive evaluation, NDT E Int. 38 (2005) 701–711.
[26] P. Lukacs, G. Davis, T. Stratoudaki, S. Williams, C.N. MacLeod, A. Gachagan, Remote ultrasonic imaging of a wire arc additive manufactured Ti-6Al-4V component using laser induced phased array, in: 2021 IEEE International Instrumentation and Measurement Technology Conference (I2MTC), 2021, pp. 1–6.
[27] R. Biswal, X. Zhang, M. Shamir, A. Al Mamun, M. Awd, F. Walther, A.K. Syed, Interrupted fatigue testing with periodic tomography to monitor porosity defects in wire+ arc additive manufactured Ti-6Al-4V, Addit. Manuf. 28 (2019) 517–527.
[28] R. Fu, S. Tang, J. Lu, Y. Cui, Z. Li, H. Zhang, T. Xu, Z. Chen, C. Liu, Hot-wire arc additive manufacturing of aluminum alloy with reduced porosity and high deposition rate, Mater. Des. 199 (2021) 109370.
[29] F. Wang, S. Williams, P. Colegrove, A.A. Antonysamy, Microstructure and mechanical properties of wire and arc additive manufactured Ti-6Al-4V, Metall. Mater. Trans. A 44 (2) (2013) 968–977.
[30] C. Fu, Y. Guo, Three-dimensional temperature gradient mechanism in selective laser melting of Ti-6Al-4V, J. Manuf. Sci. Eng. 136 (6) (2014).
[31] M. Goueygou, B. Piwakowski, A. Fnine, M. Kaczmarek, F. Buyle-Bodin, NDE of two-layered mortar samples using high-frequency Rayleigh waves, Ultrasonics 42 (1–9) (2004) 889–895.
[32] T. Stratoudaki, M. Clark, P.D. Wilcox, Full matrix capture and the total focusing imaging algorithm using laser induced ultrasonic phased arrays, AIP Conf. Proc. 1806 (1) (2017) 020022.
[33] Y. Song, X. Zi, Y. Fu, X. Li, C. Chen, K. Zhou, Nondestructive testing of additively manufactured material based on ultrasonic scattering measurement, Measurement 118 (2018) 105–112.
[34] B.W. Drinkwater, P.D. Wilcox, Ultrasonic arrays for non-destructive evaluation: a review, NDT E Int. 39 (7) (2006) 525–541.
[35] L.R.F. Rose, Point-source representation for laser-generated ultrasound, J. Acoust. Soc. Am. 75 (1984) 723–732.
[36] S. Cantero-Chinchilla, P.D. Wilcox, A.J. Croxford, A deep learning based methodology for artefact identification and suppression with application to ultrasonic images, NDT E Int. 126 (2022) 102575.
[37] B. Pouet, A. Wartelle, S. Breugnot, Multi-channel random-quadrature receiver for industrial laser-ultrasonics, in: 2011 IEEE International Ultrasonics Symposium, 2011, pp. 1809–1812.
[38] N. Maharjan, W. Zhou, Y. Zhou, Y. Guan, Ablation morphology and ablation threshold of Ti-6Al-4V alloy during femtosecond laser processing, Appl. Phys. A 124 (2018) 1–10.
[39] S.C. Wooh, Y. Shi, Optimum beam steering of linear phased arrays, Wave Motion 29 (1999) 245–265.
[40] L. Couret, N. Paul, Method, device and program for ultrasonic detection of defects in a material (French patent number FR2013483), Institut National de la Propriété Industrielle (INPI), 2020, https://patents.google.com/patent/WO2022129805A1/en.
[41] S. Hunziker, S.P. Quanz, A. Amara, M.R. Meyer, PCA-based approach for subtracting thermal background emission in high-contrast imaging data, Astron. Astrophys. 611 (2018) A23.
[42] D. Alleyne, P. Cawley, A two-dimensional Fourier transform method for the measurement of propagating multimode signals, J. Acoust. Soc. Am. 89 (3) (1991) 1159–1168.
[43] Z. Tian, L. Yu, Lamb wave frequency–wavenumber analysis and decomposition, J. Intell. Mater. Syst. Struct. 25 (9) (2014) 1107–1123.
[44] J. Camacho, M. Parrilla, C. Fritsch, Phase coherence imaging, IEEE Trans. Ultrason. Ferroelectr. Freq. Control 56 (5) (2009) 958–974.
[45] J. Camacho, C. Fritsch, J. Fernandez-Cruza, M. Parrilla, Phase coherence imaging: principles, applications and current developments, Proc. Meet. Acoust. 38 (1) (2019) 055012.
[46] G. Rousseau, A. Blouin, Hadamard multiplexing in laser ultrasonics, Opt. Express 20 (2012) 25798–25816.
[47] X. Kou, C. Pei, T. Liu, S. Wu, T. Liu, Z. Chen, Noncontact testing and imaging of internal defects with a new laser-ultrasonic SAFT method, Appl. Acoust. 178 (2021) 107956.
[48] G. Rougeron, J. Lambert, E. Iakovleva, L. Lacassagne, N. Dominguez, Implementation of a GPU accelerated total focusing reconstruction method within CIVA software, in: AIP Conference Proceedings, vol. 1581, American Institute of Physics, 2014, pp. 1983–1990.